remote sensing

MDPI

Article

Impact of Aerosol Property on the Accuracy of a CO_2 Retrieval Algorithm from Satellite Remote Sensing

Yeonjin Jung [1], Jhoon Kim [1,*], Woogyung Kim [1], Hartmut Boesch [2,3], Hanlim Lee [4], Chunho Cho [5] and Tae-Young Goo [5]

1 Department of Atmospheric Sciences, Yonsei University, 50, Yonsei-ro, Seodaemun-gu, Seoul 03722, Korea; clover529@yonsei.ac.kr (Y.J.); woolal86@yonsei.ac.kr (W.K.)
2 Earth Observation Science Group, Department of Physics & Astronomy, University of Leicester, University Road, Leicester LE1 7RH, UK; hb100@leicester.ac.uk
3 National Centre for Earth Observation, University of Leicester, University Road, Leicester LE1 7RH, UK
4 Department of Spatial Information Engineering, Pukyong National University, 45, Yongso-ro, Nam-gu, Pusan 48513, Korea; hlee@pknu.ac.kr
5 National Institute of Meteorological Sciences, 33, Seohobuk-ro, Seogwipo-si, Jeju 63568, Korea; choch0704@korea.kr (C.C.); gooty@korea.kr (T.-Y.G.)
* Correspondence: jkim2@yonsei.ac.kr; Tel.: +82-2-2123-5682; Fax: +82-2-365-5163

Academic Editors: Richard Müller and Prasad S. Thenkabail
Received: 5 January 2016; Accepted: 4 April 2016; Published: 12 April 2016

Abstract: Based on an optimal estimation method, an algorithm was developed to retrieve the column-averaged dry-air mole fraction of carbon dioxide (XCO_2) using Shortwave Infrared (SWIR) channels, referred to as the Yonsei CArbon Retrieval (YCAR) algorithm. The performance of the YCAR algorithm is here examined using simulated radiance spectra, with simulations conducted using different Aerosol Optical Depths (AODs), Solar Zenith Angles (SZAs) and aerosol types over various surface types. To characterize the XCO_2 retrieval algorithm, reference tests using simulated spectra were analysed through *a posteriori* XCO_2 retrieval errors and averaging kernels. The *a posteriori* XCO_2 retrieval errors generally increase with increasing SZA. However, errors were found to be small (<1.3 ppm) over vegetation surfaces. Column averaging kernels are generally close to unity near the surface and decrease with increasing altitude. For dust aerosol with an AOD of 0.3, the retrieval loses its sensitivity near the surface due to the influence of atmospheric scattering, with the peak of column averaging kernels at ~800 hPa. In addition, we performed a sensitivity analysis of the principal state vector elements with respect to XCO_2 retrievals. The reference tests with the inherent error of the algorithm showed that overall XCO_2 retrievals work reasonably well. The XCO_2 retrieval errors with respect to state vector elements are shown to be <0.3 ppm. Information on aerosol optical properties is the most important factor affecting the XCO_2 retrieval algorithm. Incorrect information on the aerosol type can lead to significant errors in XCO_2 retrievals of up to 2.5 ppm. The XCO_2 retrievals using the Thermal and Near-infrared Sensor for carbon Observation (TANSO)-Fourier Transform Spectrometer (FTS) L1B spectra were biased by 2.78 ± 1.46 ppm and 1.06 ± 0.85 ppm at the Saga and Tsukuba sites, respectively. This study provides important information regarding estimations of the effects of aerosol properties on the CO_2 retrieval algorithm. An understanding of these effects can contribute to improvements in the accuracy of XCO_2 retrievals, especially combined with an aerosol retrieval algorithm.

Keywords: CO_2 retrieval; GOSAT; aerosol; FTS

1. Introduction

Atmospheric Carbon Dioxide (CO_2) is one of the long-lived greenhouse gases along with methane (CH_4) and nitrous oxide (N_2O) with a lifetime in the atmosphere of decades or longer [1]. Among

these gases, CO_2 exhibits the largest radiative forcing on climate change [1], thus underpinning the importance of understanding the global carbon cycle and CO_2 sources and sinks. The concentrations of global atmospheric CO_2 have increased rapidly (by ~120 ppm) over the last 250 years, due largely to the influence of human activities, such as fossil fuel combustion and land use changes [1]. Although surface CO_2 monitoring networks have expanded in recent decades in an effort to more fully understand the global carbon cycle, these observations remain insufficient due to limitations of the spatial coverage required to identify and quantify CO_2 sources and sinks. These limitations lead to large uncertainties in climate predictions [2].

Satellite measurements are one of the most effective approaches for improving the spatial coverage and resolution of data used to monitor the distribution of greenhouse gases, and such measurements are expected to enhance the accuracy of estimations of CO_2 sources and sinks [3]. Two types of observations have been used to measure atmospheric CO_2 from satellite remote sensing: (1) Thermal Infrared (TIR) observations, such as the Atmospheric InfraRed Sounder (AIRS) on-board the Aqua satellite [4]; and (2) Short-Wavelength Infrared (SWIR) observations e.g., by the Scanning Imaging Absorption spectroMeter for Atmospheric CHartographY (SCIAMACHY) on-board the Envisat satellite [5,6]. The TIR observations are effective for detecting CO_2 concentrations in the middle to upper troposphere, while SWIR observations are sensitive to CO_2 concentration near the surface. Because CO_2 sources and sinks are mainly near the Earth's surface, the SWIR observations are more appropriate than the TIR observations for monitoring CO_2 sources and sinks. Although SCIAMACHY was not specifically designed to monitor CO_2 concentrations, it was the first satellite to measure the global distribution of CO_2 concentrations near the surface from space. However, the retrieval accuracy of SCAIAMCHY is still not sufficient to estimate CO_2 sources and sinks, for which a precision of better than 1% is required [7].

The Greenhouse gases Observing SATellite (GOSAT) was launched on 23 January 2009 to monitor the global distribution of greenhouse gases from space [8]. The Thermal And Near-infrared Sensor for carbon Observation (TANSO) instrument on-board GOSAT consists of a Fourier Transform Spectrometer (FTS) and a Cloud and Aerosol Imager (CAI). The FTS measures greenhouse gas concentrations over the troposphere at high spectral resolutions, from SWIR (0.76, 1.6 and 2.0 μm) to TIR (5.5–14.3 μm), and the CAI measures aerosol properties for the CO_2 retrieval. More detailed descriptions of the TANSO-FTS and -CAI are presented in Kuze *et al.* [9].

Several different groups have developed CO_2 retrieval algorithms, including the National Institute for Environment Studies (NIES) [10–14], the Jet Propulsion Laboratory (JPL) of the National Aeronautics and Space Administration (NASA) [15,16], the University of Leicester (UoL) [17,18], the Netherlands Institute for Space Research (SRON) and Karlsruhe Institute of Techonology (KIT) [19–21], and the University of Bremen [22]. NIES has provided standard products using an operational algorithm, while the other groups have provided research products using their own algorithms. The algorithms developed by different institutions to retrieve CO_2 concentrations are based on a general inverse method, but using different approaches and different sets of *a priori* information and aerosol models. The inverse method, which has been widely used in CO_2 retrievals, is based on an optimal estimation method, which finds a weighted mean value of the actual state and an *a priori* state. The use of an *a priori* constraint is critical to the solution of the problem. However, for retrievals, finer descriptions and an explicit *a priori* state are necessary to retain the measured information [23].

Despite the development of various CO_2 retrieval algorithms, limitations still remain regarding their spatial coverage and retrieval uncertainties, due to the presence of aerosols and optically thin cirrus clouds. Even under clear-sky condition, only ~10% of the total daytime sounding is passing post-processing quality filters [24]. Furthermore, already a small amount of aerosols or cirrus clouds at high altitudes can introduce biases in CO_2 retrievals, because of uncertainties in the modification of the optical path [24,25]. Although the effects of aerosols and cirrus clouds can be treated by using the O_2-A band, this band provides information on the amount and distribution of the aerosols and not on

the aerosol optical properties. In other words, more accurate information on the properties of aerosols and clouds is required to improve the accuracy of CO_2 retrievals.

The GOSAT operational algorithm assumes that two types of aerosols are uniformly distributed below 2 km without cirrus clouds and with fixed information for aerosol optical properties from the Spectral Radiation Transport Model for Aerosol Species (SPRINTARS), instead of aerosol measurements from the CAI. As this assumption about aerosols depends on model simulations, its uncertainty may result in significant errors in the CO_2 retrievals. Over East Asia where a large amount of aerosols and clouds are present throughout the year, optimized retrieval algorithms are required to handle their effect carefully. Therefore, to further improve the retrieval accuracy, it will be necessary to develop and test an alternative method for obtaining aerosol information in the CO_2 retrievals.

The Yonsei CArbon Retrieval (YCAR) algorithm, developed by Yonsei University, retrieves the column-averaged CO_2 mole fraction (XCO_2), which is based on an algorithm developed by UoL (UoL Full Physics, UoL-FP) [17,18]. However, the two algorithms differ in terms of the *a priori* CO_2 information and the aerosol models. In our retrieval algorithm, Carbon Tracker-Asia (CT-Asia) data are used as *a priori* CO_2 profiles over East Asia; CT-Asia is optimized to provide high spatial resolution and high accuracy data for the Asian region. In addition, as stated above, to reduce the model parameter errors caused by the assumption of aerosol information, the climatology of ground-based optical measurements, the AErosol RObotic NETwork (AERONET), is used as *a priori* data in the retrieval algorithm.

In this study, the performance of a new CO_2 retrieval algorithm is assessed and its sensitivity is analysed using simulated radiance spectra for different surface and atmospheric conditions. Specifically, the CO_2 retrieval errors and column averaging kernels are analysed to examine the retrieval accuracy, and the effects of respective state vector elements on CO_2 retrieval are evaluated. Furthermore, the retrievals are conducted using real spectra from the TANSO-FTS and validated with ground-based measurements to examine the accuracy of the algorithm.

The remainder of this paper is organized as follows. Section 2 briefly describes our CO_2 retrieval algorithm, and Section 3 presents an analysis of the sensitivities of the XCO_2 retrieval errors to each state vector element. Section 4 describes the retrieval conditions and shows the retrieval results in comparison with ground-based measurements. Finally, a discussion and summary are presented in Section 5. This study provides a detailed assessment of aerosol effects on XCO_2 retrievals, by using simulated information on aerosol optical properties. This approach will eventually contribute to an improved and more accurate XCO_2 algorithm for TANSO-FTS using aerosol information derived from the TANSO-CAI on-board the same platform.

2. Retrieval Algorithm

The YCAR algorithm was developed to retrieve XCO_2 from SWIR radiance spectra. The retrieval method is based on an optimal estimation approach, in which input parameters, referred to as state vectors ($\boldsymbol{x}$), are optimized to yield simulated spectra that are close to the measured spectra, as simultaneously constrained by *a priori* information with a suitable error covariance [23]. This retrieval method allows other parameters to be selected and retrieved from atmospheric, surface and instrumental characteristics and can also be applied to inversions of other satellite sensors.

The flow chart of the YCAR algorithm is shown in Figure 1. The retrieval process begins such that the initial guess and the *a priori* values for the state vectors are identical. Using a pre-calculated covariance matrix for the state vectors, a forward model generates synthetic radiance spectra and the Jacobian, which is the derivative of the radiance spectra with respect to each state vector, for the O_2 A-band at 0.76 μm and the two CO_2 absorption bands centred at 1.6 and 2.0 μm [10]. The bands and the spectral ranges used in the retrieval algorithm are summarized in Table 1. Using an inverse model that is coupled with the forward model, the initial state vector is modified by minimizing the difference between the simulated and observed radiance spectra through iteration. The remainder of this section describes each component of the retrieval algorithm.

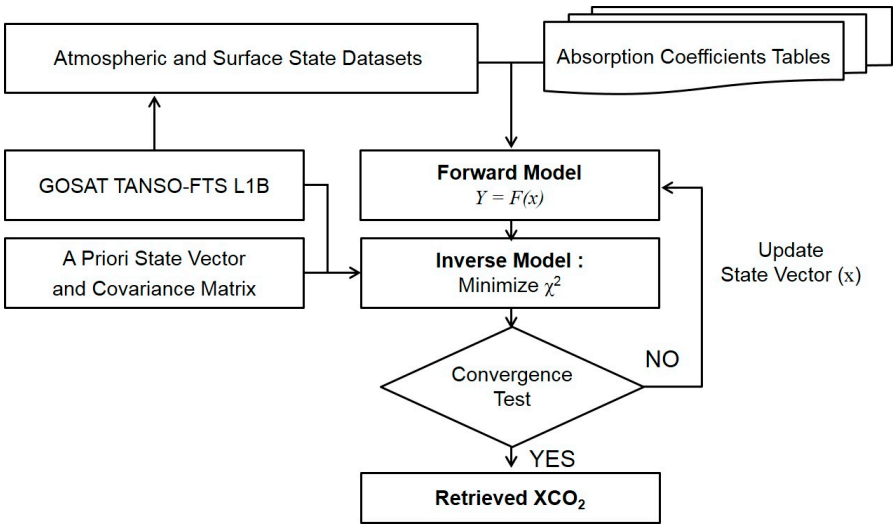

Figure 1. The flow chart of the Yonsei CArbon Retrieval (YCAR) algorithm.

Table 1. The spectral band used in the YCAR algorithm.

Band Number	Spectral Range	Number of Channels
1	12,950–13,200.6 cm^{-1} (0.757–0.772 μm)	1256
2	6161.0–6297.4 cm^{-1} (1.588–1.623 μm)	684
3	4800.0–4902.2 cm^{-1} (2.040–2.083 μm)	512

2.1. State Vectors

The state vector elements are physical quantities that influence the radiance spectra and are optimized and retrieved parameters in the inverse method. The state vectors include CO_2 volume-mixing ratio profiles, a scaling factor of the H_2O profile, the surface albedo for each band over land, aerosol optical depth (AOD) profiles at 0.76 μm, surface pressure, offsets of the temperature profile and the wavenumber shift and squeeze as auxiliary parameters (which are also retrieved simultaneously). The state vector elements and the *a priori* data used in our retrieval algorithm are listed in Table 2.

The atmospheric layer is divided into 20 levels from the surface to 0.1 hPa, using a constant pressure grid, and where XCO_2 is retrieved as a vertical profile of the dry-air mole fraction defined at each pressure level. The *a priori* CO_2 profiles are obtained from CT-Asia, with a spatial resolution of $1^\circ \times 1^\circ$ and a temporal resolution of 3 h [26]. The Carbon Tracker (CT) is a CO_2 measurement and modelling system developed by the National Oceanic and Atmospheric Administration (NOAA) to keep track of sources and sinks of CO_2 globally [27]. Although the CT-Asia and CT are similar to one another, these two models show some differences, including the transport resolution and the planetary boundary-layer (PBL) scheme. The CT-Asia uses a nested grid to provide enhanced transport resolution over Asia instead of over North America. In addition, its vertical diffusion scheme has been changed to the Yonsei University (YSU) PBL scheme [28], which has greater vertical mixing, diffusing CO_2 in the PBL instead of trapping it in the surface layer. In particular, CT-Asia uses an observation dataset supported by the Japan Meteorological Agency (JMA) that is not assimilated into the CT, with fluxes optimized to match surface observations over East Asia. CO_2 covariance defined on the prescribed 20 pressure levels is calculated at each level over East Asia from CT-Asia during 2010–2012, as shown in Figure 2. The total *a priori* uncertainty is largest near the surface and decreases

with increasing altitude. To avoid strong constraints on the *a priori* profiles, the calculated *a priori* uncertainties of the CO_2 profiles were multiplied by a factor of 100 and used in the retrieval algorithm.

Table 2. State vector composition of the YCAR algorithm. ECMWF, European Centre for Medium-Range Weather Forecasts; AOD, Aerosol Optical Depth.

Name	Quantity	Description	*A Priori*	*A Priori* 1-σ Error
CO_2	20 levels	Volume mixing ratio on each level	Carbon Tracker-Asia	Fixed matrix as seen in Figure 2
H_2O	1	Multiplier to *a priori* profile	ECMWF	0.5
Temperature	1	Offset to *a priori* profile	ECMWF	5 K
Aerosols	19 layers (3 types)	AOD profiles on each level for user-defined types	Constant	0.5 of a priori profiles
Surface albedo	3 bands × 2 variables	Albedo at band centre Albedo slope	From spectrum	1 $0.0005/cm^{-1}$
Wavenumber	3 bands × 2 variables	Wavenumber shift Wavenumber squeeze	From spectrum	$1\ cm^{-1}$ $1.0 \times 10^{-5}\ cm^{-1}$

The *a priori* profiles of H_2O, temperature and surface pressure are derived from the European Centre for Medium-Range Weather Forecasts (ECMWF) ERA-Interim dataset, which has a temporal resolution of three hours and a horizontal resolution of $0.125^\circ \times 0.125^\circ$. The *a priori* profiles of H_2O, temperature and surface pressure at a given latitude, longitude and altitude are interpolated on a fixed pressure grid. Because the H_2O profiles vary according to region, it is assumed that the *a priori* H_2O profiles are accurate and realistic, so as to reduce the uncertainties of the profiles. Under this assumption, the H_2O profiles can be expressed by scaling factors of the *a priori* H_2O profiles. For the temperature profiles, the offset of *a priori* profiles is set as a state vector parameter. The temperature profiles are allowed to vary with constant offsets, so that variations in the temperature profiles have little influence on the retrievals. The *a priori* 1-σ uncertainty of the scaling factor of the H_2O profiles and the temperature offset were set to 0.5 and 5 K, respectively. Surface pressure derived from ECMWF has biases of <1 hPa globally. However, larger biases occur over the high-latitude Southern Ocean (2 hPa), and positive biases as large as 3–4 hPa occur in some higher-altitude regions over Asia [29]. Therefore, to avoid strong constraints on the *a priori* information, the *a priori* 1-σ uncertainty of surface pressure was set at 4 hPa, as reported by O'Dell *et al.* [16]. In this study, surfaces over land are assumed to be purely Lambertian. The spectral dependence of surface albedo is expressed using two parameters, representing the value at the centre wavenumber of each band and its slope within the wavenumber range, so as to reduce the number of state vector elements. Because these parameters are essentially unconstrained, the covariance of these parameters was set to a large value, using a surface albedo at the centre wavenumber of one and a slope of $0.0005/cm^{-1}$ [16]. *A priori* values of the surface albedo were estimated from TANSO-FTS spectra during the pre-processing, and *a priori* values of its slope at each band were set to zero.

To represent atmospheric scattering, the AOD profiles for 19 atmospheric layers were considered as state vectors. In our retrieval algorithm, *a priori* total AOD values are set to 0.05 because our retrievals focused only on cloud-free measurement scenes. The aerosol *a priori* profiles were determined in the forward model, according to the peak height and half-width of the shape of the assumed aerosol vertical profiles. It is assumed that aerosol profiles can vary by up to 50% of the value of the *a priori* aerosol profile. In our retrieval algorithm, the parameters used to represent aerosol optical properties in the forward model were not considered as state vectors, but rather as fixed variables introduced in an iterative process. Therefore, the assumption of aerosol optical properties is very important for representing aerosol properties, because inaccurate aerosol optical information can cause retrieval errors. To obtain an optimized aerosol model over East Asia and to reduce errors, the extensive inversion products of the AERONET dataset over East Asia (100°–160°E, 10°–60°N) were analysed [30]. As reported by Kim *et al.* [31] and Lee *et al.* [32], aerosols in the atmosphere can be characterized by

their radiation absorptivity and size and can be classified into four major types: Black Carbon (BC), dust, Non-Absorbing (NA) and mixtures. The classification algorithm of aerosols is robust, although its performance depends on threshold values to determine the aerosol types. The dominant size mode was determined as the fine mode fraction (FMF) at 0.5 μm and absorbing aerosols can be distinguished from non-absorbing aerosols by Single Scattering Albedo (SSA). According to this method, Black Carbon (BC) is the most frequently classified aerosol type over East Asia. Each aerosol type has an assumed particle size distribution and refractive index, as listed in Table 3.

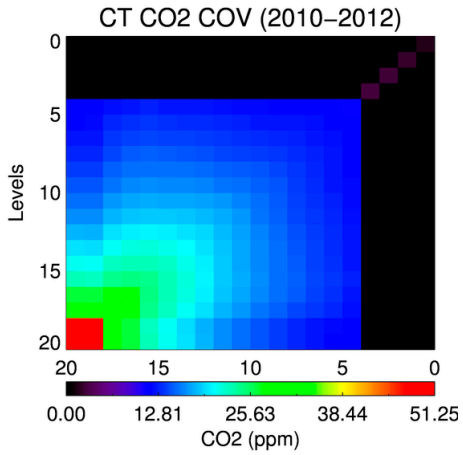

Figure 2. *A priori* covariance matrix derived from Carbon Tracker-Asia during 2010–2012 over East Asia. The colours represent the 1-σ value between CO_2 mixing ratios at different levels, which is multiplied by a factor of 100. Levels are arranged from TOA to surface as 1–20.

Table 3. Aerosol number-size distribution parameters and refractive index for each aerosol type in the YCAR algorithm. Number size distribution parameters are radius (r_{m1}, r_{m2}) and variance (σ_{m1}, σ_{m2}) for fine and coarse and fine mode fraction (FMF), respectively. The real and imaginary parts of the refractive index for each aerosol type are n_{real} and n_{img}, respectively.

Aerosol Type	r_{m1}	r_{m2}	σ_{m1}	σ_{m2}	FMF	n_{real}	n_{img}
BC	0.076	0.624	1.677	2.008	0.999	1.486	0.010
Dust	0.041	1.103	2.370	1.647	0.995	1.546	0.002
NA	0.088	0.664	1.777	1.955	0.999	1.426	0.004

2.2. Forward Model

The forward model simulates the radiance spectra and calculates Jacobians, which are the derivatives of the simulated radiance spectra with respect to each state vector. Mathematically, the simulations of observed radiance spectra (y) from state vectors ($\boldsymbol{x}$) can be expressed as follows:

$$y = F(x, b) + \varepsilon \quad (1)$$

where $F(x)$ is the radiance spectra simulated by the forward model using the state vector (x), b is fixed input parameters and ε contains the instrument noise and forward model errors. For GOSAT TANSO-FTS, the instrument noise is derived from the standard deviation of the out-of-band radiance at each band. In this study, geometric information for the selected TANSO-FTS L1B spectrum was used as examples, and the instrument noise was calculated from selected TANSO-FTS L1B spectra. The main objective of this study is a theoretical analysis of the retrieval algorithm, and thus, no forward model errors are assumed in the retrieval algorithm.

The forward model consists of three models: a radiative transfer model, a solar model and an instrument model. The radiative transfer model includes a radiative transfer module, an atmospheric

module and surface modules. The radiative transfer module used in this study is the Vector Linearized Discrete Ordinate Radiative Transfer (VLIDORT) Version 2.6 [33]. The atmospheric module takes into account atmospheric and gas profiles, aerosols and cloud and calculates their optical properties as required for the radiative transfer module. At prescribed pressure levels, each gas profile is converted into an absorption optical depth, using an absorption coefficient for each gas. In this study, ABSorption COefficient (ABSCO) tables provided by the JPL were used to calculate the absorption cross-section for each gas [34]. The ABSCO tables contain absorption cross-section values for each of the absorbing gases as a function of pressure, temperature and wavenumber [35]. The ABSCO tables also include line-mixing and collision-induced absorption, which are considered necessary for accurate retrievals of CO_2 using near-infrared solar spectra [36]. The atmospheric module also includes scattering processes. As reported by Bodhaine *et al.* [37], Rayleigh scattering is parameterized in a way that the Rayleigh optical depth is a simple function of wavelength and atmospheric number density. Aerosols and their extinction profiles are converted to optical depth at each wavenumber. To calculate composite optical depth, single scattering albedo and scattering phase matrix values, the optical properties of gases, aerosols and Rayleigh are combined and input into the atmospheric transfer module. For the surface model, we assumed that the surface can be perfectly represented as a simple Lambertian surface and that surface albedo varies linearly with wavenumber across the three SWIR bands, as stated above.

After determining the atmospheric optical properties and surface reflectance properties, the monochromatic radiance spectra at the top-of-atmosphere were simulated at high resolution (0.01 cm^{-1}). The spectral resolution of the radiative transfer model must be finer than the spectral resolution of the TANSO-FTS of 0.2 cm^{-1} to simulate the radiance spectra. The spectral regions used in the radiative transfer model cover the O_2-A absorption band centred at 0.76 μm and CO_2 absorption bands centred at 1.6 and 2.0 μm. Because the radiance spectra simulated by the radiative transfer model yield an initially dimensionless reflectance, the high-resolution radiance spectra calculated by the radiative transfer model are multiplied by the high-resolution solar spectrum in the solar model. The solar model consists of a solar absorption model and a continuum model. The solar absorption model calculates the solar line list generated by simultaneous fitting of different high-resolution FTS spectra and balloon observation created by Geoff Toon (http://mark4sun.jpl.nasa.gov/toon/solar/solar_spectrum.html): Atmospheric Trace MOlecule Spectroscopy (ATMOS) in the range of 600–4800 cm^{-1}, the MkIV balloon spectra in the range of 650–5650 cm^{-1}, the Kitt Peak ground-based spectra in the range of 3800–25,000 cm^{-1}, the Denver University balloon spectra in the range of 12,900–13,200 cm^{-1} and the Total Carbon Column Observing Network (TCCON) spectra from Park Falls in the range of 3900–15,000 cm^{-1}. The solar model includes both disk centre and disk-integrated line lists. The line list can be used to generate high-resolution solar pseudo-transmittance spectra in the range of 600–25,000 cm^{-1}. The solar continuum model is calculated using a ninth order polynomial fitting to the near-infrared part of the low-resolution extra-terrestrial solar spectrum, measured by the SOLar SPECtrum (SOLSPEC) instrument [38]. To obtain the high-resolution solar spectrum, the solar continuum model was multiplied by the solar absorption model.

In the instrument model, the simulated monochromatic high-resolution radiance spectra are convolved with the low-resolution measured wavenumber using the instrument line shape function (ILS) of the TANSO-FTS. The ILS model of the TANSO-FTS bands was provided by the GOSAT data centre (https://data.gosat.nies.go.jp/gateway/gateway/MenuPage/open.do). Integration over the radiance spectrum was performed over a 100-cm^{-1} range, centred at each band.

2.3. Inverse Model

The solution of the retrieval algorithm is a state vector ($\boldsymbol{x}$) with a maximum *a posteriori* probability. Our inverse method employs the Levenberg–Marquardt modification of the Gauss–Newton method, which is used to minimize the cost function between measured and simulated radiance spectra [23]. To find the state vector with maximum *a posteriori* probability, the cost function (χ^2) is minimized as follows:

$$\chi^2 = [y - F(x)]^T S_\varepsilon^{-1}[y - F(x)] + [x_a - x]^T S_a^{-1}[x_a - x] \quad (2)$$

where x_a is an *a priori* state vector, $F(x)$ is simulated radiance spectra calculated using the forward model with the state vector (x), S_ε is the measurement error covariance matrix, S_a is the *a priori* covariance matrix and the superscript T represents the matrix transpose. To find the solution, the updated state vectors (x_{i+1}) were estimated using the following iterative equation at each step:

$$x_{i+1} = x_i + [K_i^T S_\varepsilon^{-1} K_i + (1+\gamma) S_a^{-1}]^{-1}[K_i^T S_\varepsilon^{-1}(y - F(x_i)) + S_a^{-1}(x_a - x_i)] \quad (3)$$

where subscript i denotes the i-th iteration, $F(x_i)$ is the simulated radiance spectra calculated using the forward model with state vector (x_i) at the i-th iteration step, $\boldsymbol{K_i} = \frac{\partial \boldsymbol{F}(x_i)}{\partial \boldsymbol{x_i}}$ is the corresponding weighting function (Jacobian) and γ is the Levenberg–Marquardt parameter. The value of γ is initially set to 10.0, but can be changed according to the R value, which is the ratio of the actual reduction in the cost function to the forecast reduction in the cost function, with the assumption of linearity, expressed as:

$$R = \frac{\chi_i^2 - \chi_{i+1}^2}{\chi_i^2 - \chi_{i+1(FC)}^2} \quad (4)$$

where FC denotes the forecast value. In this step, if the updated amount of the state vector is less than 1-σ of the *a priori* value, then convergence is reached. The inverse model is iteratively processed until convergence criteria are satisfied. We used the R value and the convergence criteria of Crisp *et al.* [34]. To examine the retrievals, the difference between the retrieved and true value of the CO_2 concentration, referred to as the XCO_2 retrieval error in this study, and its column averaging kernels were analysed, as presented in the next section.

3. Retrieval Sensitivity Results Using Simulated Spectra

3.1. Simulations of TANSO-FTS Spectra

In this study, a set of input parameters, including surface albedo, Solar Zenith Angle (SZA) and total AOD, were utilized to simulate realistic radiance spectra. These parameters considerably change the radiance and, thus, affect the retrieval errors and averaging kernels. The ranges of the parameters used to simulate the spectra are listed in Table 4. All simulations were conducted under conditions of nadir observations and a relative azimuth angle of 45°.

Table 4. Range of parameters used for simulations.

Parameter	Range
Total AOD	0.01, 0.05, 0.10, 0.15, 0.20, 0.25, 0.30
Solar zenith angle	10, 20, 30, 40, 50, 60
Surface type	Vegetation, Snow, ocean

For the simulations, three different surface types (e.g., vegetation, snow and ocean) were selected, and a Lambertian surface was considered. In the simulation, *a priori* values of spectral surface albedo over vegetation (conifer) and snow surfaces were taken from the Advanced Space-borne Thermal Emission Reflection Radiometer (ASTER) Library [39]. The Lambertian albedo over the ocean surface was set to 1% for all three spectral bands [17]. When using the ASTER library, the slope of the surface was calculated as the ratio of the differences in surface albedo and wavenumber difference from the wavenumber centre over the full wavenumber range.

Atmospheric aerosol profiles were represented by a Gaussian shape profile, with a peak height of 0.1 km and a half width of 1 km below 5 km to obtain a vertically-integrated AOD, using AOD values

in the range of 0.01–0.30 at 0.76 μm. As stated above, our retrieval algorithm includes three aerosol types (BC, dust and NA) that are reflected in the forward model as fixed model parameters.

3.2. XCO_2 Retrieval Errors and Averaging Kernels

To evaluate the basic characteristics of the retrieval algorithm developed in this study, a reference test was conducted under the assumption that the initial values of all state vectors represent true values at each AOD and SZA over each surface type. During the initial stages of development, the reference tests were used to confirm the algorithm and to estimate the basic error included in the retrieval algorithm with known solutions.

The CO_2 retrieval algorithm was characterized using two typical parameters: the XCO_2 retrieval errors and the column averaging kernels. The XCO_2 value is obtained by averaging the retrieved CO_2 vertical profiles, weighted by a pressure weighting function (h):

$$XCO_2 = h^{\mathrm{T}}\hat{x} \tag{5}$$

where h represents the pressure interval assigned to the atmospheric level, normalized by the surface pressure and corrected for the presence of water vapour, and $\hat{x}$ is the retrieved state vector. Details of the calculation of h are given by O'Dell *et al.* [16]. After reaching a convergent iterative solution, the error covariance matrix ($\hat{S}$) and averaging kernels (A) are respectively calculated as follows:

$$\hat{S} = \left(K^{\mathrm{T}} S_{\varepsilon}^{-1} K + S_a^{-1}\right)^{-1} \tag{6}$$

$$A = \frac{\partial \hat{x}}{\partial x} = \hat{S} K^{\mathrm{T}} S_{\varepsilon}^{-1} K \tag{7}$$

where x represents the state vectors. The averaging kernel matrix gives the sensitivity of the retrieval to the true profiles.

In this study, the XCO_2 retrieval errors represent the difference between retrieved XCO_2 values and assumed true values. *A posteriori* XCO_2 retrieval errors are given by the square root of the error variance in the reference test. The error variance in the retrieved XCO_2 value ($\sigma^2{}_{XCO2}$) is given by:

$$\sigma^2{}_{XCO2} = h^{\mathrm{T}} \hat{S} h \tag{8}$$

The column averaging kernels for level j $(a_{CO2})_j$ are given by:

$$(a_{CO2})_j = \frac{\partial \mathrm{XCO_2}}{\partial x_j} \frac{1}{h_j} = \left(h^{\mathrm{T}} A\right)_j \frac{1}{h_j} \tag{9}$$

The elements in the column averaging kernels are equal to unity in ideal cases, which means that the retrieved XCO_2 value responds to changes in the state vector and exactly matches the true value of the profiles. However, in real retrievals using measured spectra, the values of elements are generally <1, and thus, the *a priori* CO_2 profiles become important [18].

For the analysis of XCO_2 retrieval errors and column averaging kernels in the reference test, several assumptions were made. For each aerosol type over a different surface type, all state vectors are equal to their true profiles under cloud-free conditions. *A posteriori* XCO_2 retrieval errors obtained in the reference tests are shown in Figure 3 as a function of AOD and SZA for the assumed aerosol (BC, dust and NA) and surface (vegetation, snow and ocean) types. As shown in Figure 3, the *a posteriori* XCO_2 retrieval error generally increases with increasing SZA. Small errors are found over vegetation surfaces, with values of <1.3 ppm for all SZAs and all AODs, regardless of aerosol type. With increasing SZA, the *a posteriori* XCO_2 retrieval errors increase slightly over all surface types. As compared to *a posteriori* XCO_2 retrieval errors over vegetation and snow, the errors over the ocean show very large values. These results can be explained by the large variance in the retrieved XCO_2 values due to the low sensitivity of retrievals over the ocean surface. *A posteriori* XCO_2 retrieval errors

over the ocean surface significantly increase with increasing SZA values (by up to 14 ppm for large SZA values). On the other hand, while *a posteriori* XCO_2 retrieval errors increase with increasing AOD over vegetation and snow, regardless of the assumed aerosol type, the error decreases with increasing AOD over the ocean surface. This result can be explained by the fact that aerosol effects on XCO_2 retrievals are more significant over the ocean than over land for all SZAs, due to the low albedo over the ocean [17]; this is because the sensitivity of retrievals depends on the total AOD, especially at the surface. In addition, it is assumed in our retrievals that aerosols are mostly distributed near the surface. Therefore, the patterns of *a posteriori* XCO_2 retrieval errors over vegetation and ocean appear somewhat different from one another. More explanations related to column averaging kernels are provided in the following.

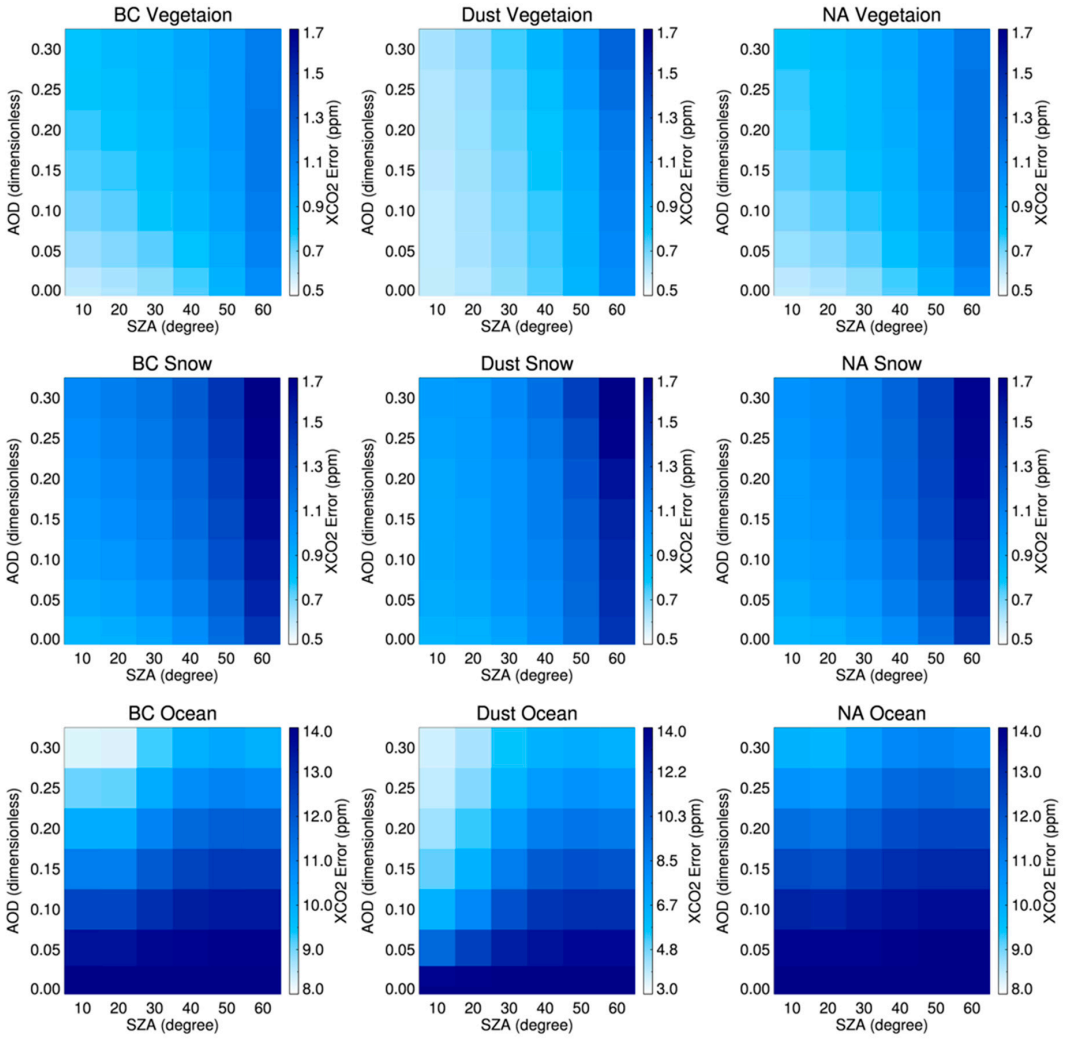

Figure 3. *A posteriori* XCO_2 retrieval errors for Black Carbon (BC) (**left** column), dust (**middle** column) and Non-Absorbing (NA) (**right** column) aerosol types as a function of AODs and Solar Zenith Angels (SZAs) for vegetation (**top** panel), snow (**middle** panel) and ocean (**bottom** panel).

The column averaging kernels were analysed at the same time as the analysis of *a posteriori* XCO_2 retrieval errors. Figure 4 shows the column averaging kernels at different SZAs for a fixed AOD value of 0.3 and for the assumed aerosol and surface types. The column averaging kernels for BC and NA aerosol types with an AOD of 0.3 show similar shape patterns, as compared to patterns under aerosol-free conditions. Figure 4 also shows that the column averaging kernels are close to unity near the surface over vegetation and snow surfaces, but decrease with decreasing pressure above ~400 hPa.

This means that the retrieval loses its sensitivity at high altitudes in the upper troposphere. It is also suggested that the column averaging kernels with respect to altitude are decreased more at higher SZAs. However, for the dust aerosol type with an AOD of 0.3, the retrievals largely lose their sensitivity near the surface, as well as compared to the sensitivity for BC and NA aerosol types. In addition, a maximum of the column averaging kernels is shown at ~800 hPa, which can be explained by the increasing influence of atmospheric scattering at this altitude. This decrease tendency near the surface appears more significant over snow as compared to over vegetation surfaces. Over the ocean surface, the column averaging kernels for all aerosol types show low values near the surface, a pattern that is closely related to the low surface albedo over the ocean.

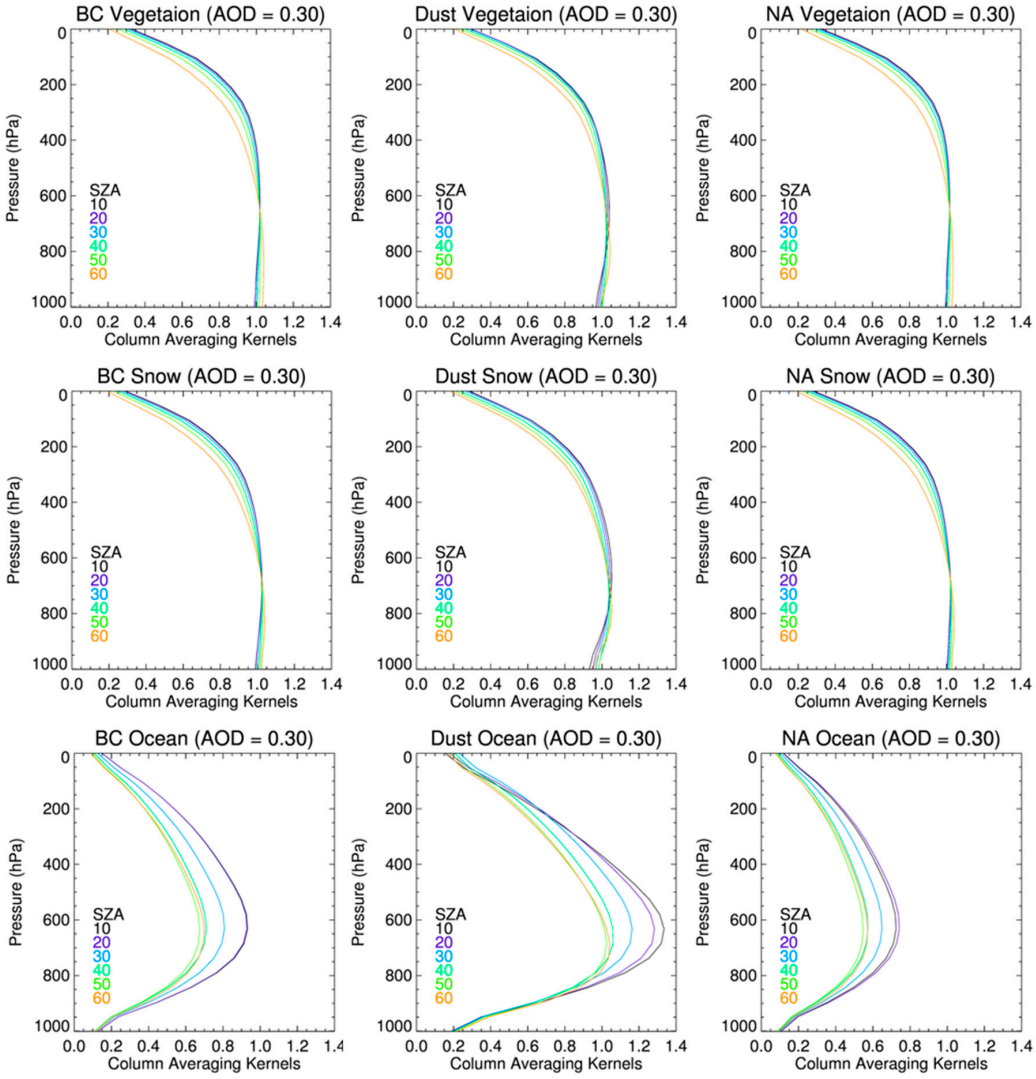

Figure 4. Column averaging kernels for BC (**left** column), dust (**middle** column) and NA (**right** column) aerosol types for an AOD of 0.3 over vegetation (**top** panel), snow (**middle** panel) and ocean (**bottom** panel).

3.3. The Sensitivity of XCO_2 Retrieval Errors to State Vector Elements

The previous section described our characterization of XCO_2 retrieval errors for datasets covering a large range of different surface types, aerosol types and AOD and SZA values. Here, we further examine the sensitivity of XCO_2 retrieval errors to perturbations of the state vector elements. The simulated conditions were fixed, with a SZA of 30° over vegetation surfaces for various total AOD

values in the range of 0.01–0.30, as shown in Table 4. Figures 5 and 6 show the XCO_2 retrieval errors for the respective values of the perturbed state vector elements.

Figure 5 shows the XCO_2 retrieval errors for respective assumed total AOD and aerosol type based on perturbed CO_2, H_2O and temperature profiles. The perturbation of CO_2 profiles was set to only a $\pm$ 2% error (~8 ppm) at the surface in initial value for CO_2 profiles, as compared to the true CO_2 profiles. To avoid large errors at upper altitudes, where the *a priori* covariance is very small, the errors at each pressure level were decreased smoothly from the surface to the top level. For the perturbed CO_2 profiles, as shown in the left column of Figure 5, the XCO_2 retrieval errors for all aerosol types were generally less than 0.2 ppm. Regardless of the assumed total AOD and aerosol type, the values of the XCO_2 retrieval errors are similar. For the dust aerosol type, the extent of the XCO_2 retrieval errors with changes in the initial CO_2 profiles was slightly greater than that of the other aerosol types. For the H_2O profile, the scaling factor of *a priori* profiles was set as a state vector with the assumption that the *a priori* profiles are a good representation of the true profiles. In this study, the perturbation of the H_2O profiles was set to $\pm$50% of the assumed true H_2O profiles. As shown in the middle column of Figure 5, the relatively large perturbation shows that the XCO_2 retrieval errors are only slightly sensitive to H_2O profiles. Although the XCO_2 retrieval errors (with a perturbation of $\pm$50% of the assumed true profiles) are larger than those obtained for the other perturbations, the errors are still small (within ~0.6 ppm). Regardless of the assumed total AOD and aerosol type, the retrieved XCO_2 is overestimated as compared to the true XCO_2 value. The XCO_2 retrieval errors obtained with the perturbations of the *a priori* temperature profiles are also shown in the right column of Figure 5. The temperature profile parameters used in the retrieval algorithm are the offsets of the initial temperature profiles. Thus, the perturbations are set to a constant value of $\pm$10 K of the initial temperature profiles. As shown in Figure 5, the patterns of the XCO_2 retrieval errors with the perturbation of *a priori* CO_2, H_2O and temperature profiles are similar to one another and are mostly <0.2 ppm. These results indicate that the state vector elements have relatively small effects on XCO_2 retrievals.

The XCO_2 retrieval errors obtained using a perturbation for total AOD and a misleading aerosol type are shown in Figure 6. This figure shows that the perturbation in total AOD is set to $\pm$50% of the *a priori* total AOD. A comparison of Figures 5 and 6 shows that the total AOD has little influence on XCO_2 retrievals and similarly for the CO_2, H_2O and temperature profiles. The XCO_2 retrieval errors also show a value of ~0.2 ppm, regardless of the total AOD for respective aerosol types. The retrieved XCO_2 values are slightly overestimated (by ~0.1 ppm), even without the perturbation in total AOD, which can be attributed to the inherent characteristics of the algorithm. In addition, inaccurate information on aerosol optical properties can result in large XCO_2 retrieval errors, as compared to those for other variables. Because aerosols in the atmosphere vary in terms of their chemical composition and particle size distribution, as well as their vertical distribution [40], assumed and fixed information of aerosol optical properties can lead to significant XCO_2 retrieval errors. Figure 6 also shows the XCO_2 retrieval errors caused by incorrect optical information on aerosol types. The results are produced under the conditions that optical information for assumed aerosol type differs with that of true aerosol type. As shown in the figure, the effects of aerosol optical properties on XCO_2 retrievals are large, as compared to the effects of other state vectors. For the BC aerosol in the atmosphere, the XCO_2 retrieval errors due to incorrect information on aerosol optical properties can increase by up to ~2.5 ppm, for example if the BC is misdetected as dust. The XCO_2 retrieval errors are also increased with increasing AOD values. Thus, the information on assumed aerosol types appears the most important factor influencing the accuracy of the XCO_2 retrievals. In contrast, as discussed above for the simulation studies, differences in the initial values of CO_2, H_2O and temperature profiles do not appear to result in significant errors in the XCO_2 retrievals. The range of XCO_2 retrieval errors with respect to state vector elements for each aerosol type for a SZA of 30° over vegetation surface is given in Table 5.

Table 5. Range of XCO_2 retrieval errors with respect to state vectors for BC, dust and NA aerosols for a SZA of 30° with respect to state. Units are in ppm.

State Vector / Aerosol Type		BC		Dust		NA	
Variables	**Errors**	**Min.**	**Max.**	**Min.**	**Max.**	**Min.**	**Max.**
CO_2	±1%–2% (±~4–8 ppm)	−0.135	−0.079	−0.156	−0.064	−0.134	−0.077
H_2O	±20%–50%	−0.537	−0.011	−0.244	0.216	−0.454	−0.031
Temperature	±10 K	−0.158	−0.086	−0.128	−0.038	−0.163	−0.082
AOD	±20%–50%	−0.189	−0.086	−0.129	−0.076	−0.151	−0.081
Aerosol type	BC, dust, NA	−0.121	2.544	−2.167	−0.076	−2.225	0.129

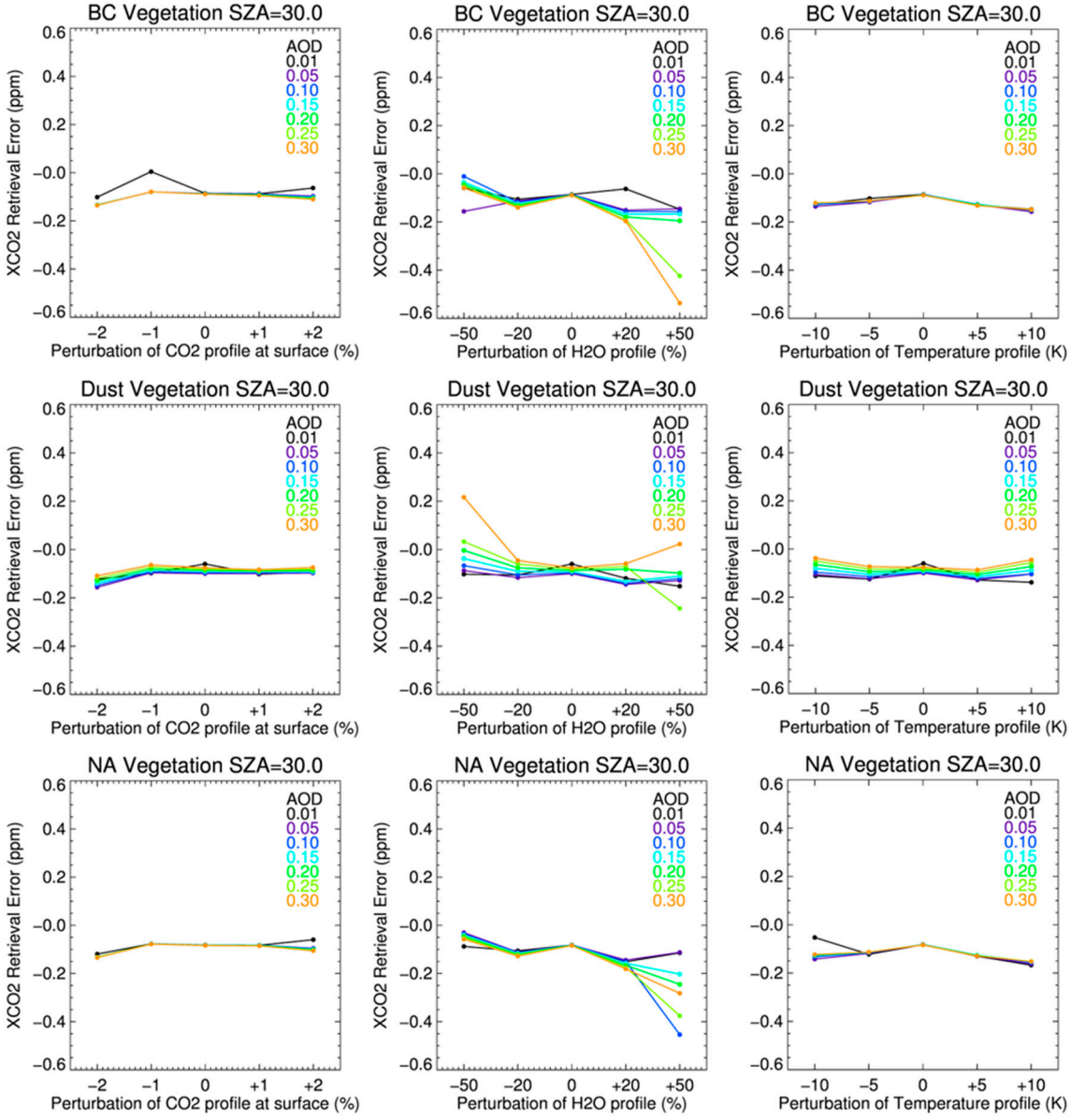

Figure 5. The XCO_2 retrieval errors for BC (**top** panel), dust (**middle** panel) and NA (**bottom** panel) aerosol type with respect to the perturbed CO_2 profiles (**left** column), H_2O profiles (**middle** column) and temperature profile (**right** column) for a SZA of 30° over vegetation, respectively.

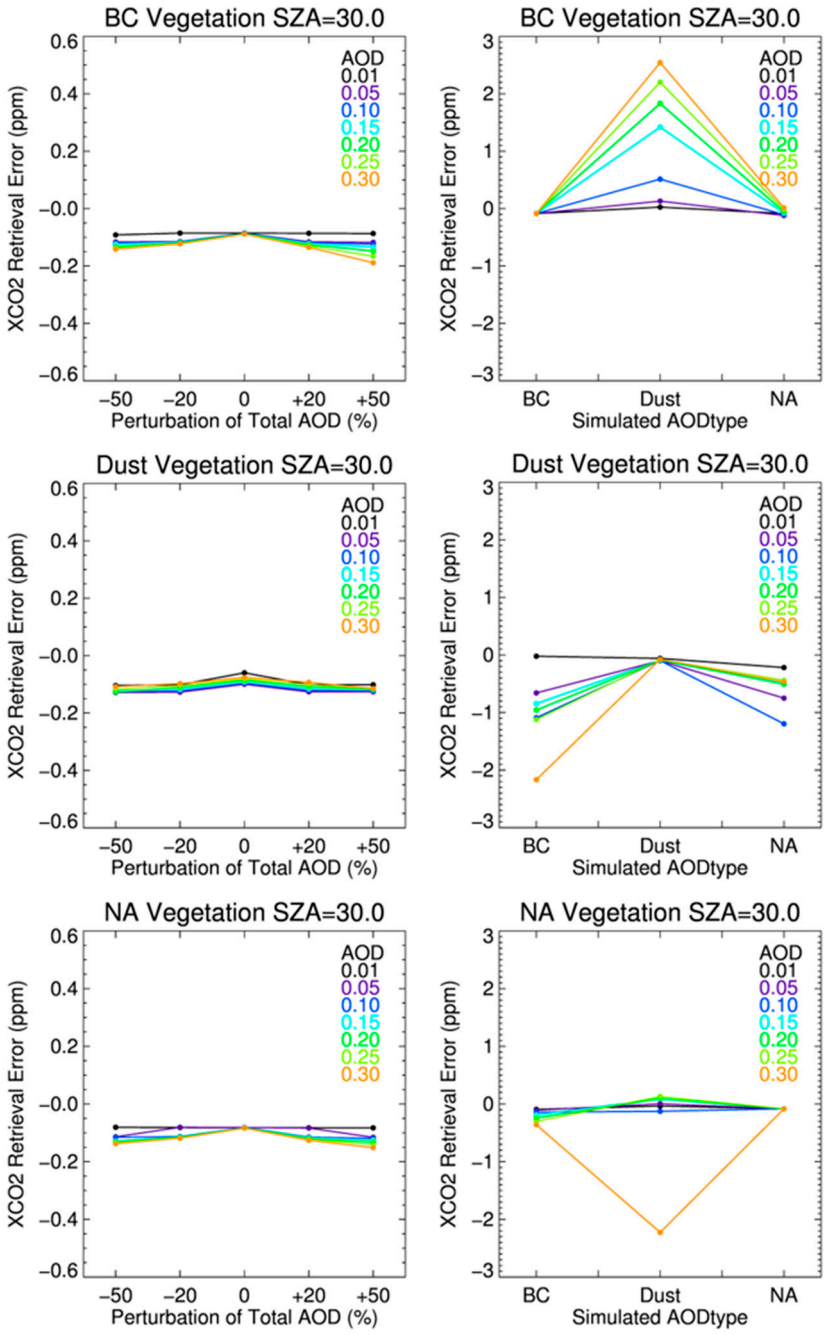

Figure 6. Same as in Figure 5, except for the perturbed total AOD (**left** column) and information in aerosol type (**right** column), respectively.

4. Preliminary Validation of XCO_2 Retrieved from GOSAT Spectra

4.1. Retrieval Conditions

This section describes the performance of our XCO_2 retrieval algorithm using real TANSO-FTS L1B spectra to evaluate the accuracy of the retrieval algorithm. The retrieval results are compared to ground-based FTS data at Saga and Tsukuba TCCON stations for the period from 2011–2012.

We used the TANSO-FTS L1B spectra Version 161.160, with the radiance degradation of TANSO-FTS corrected according to Yoshida *et al.* [41] and Kuze *et al.* [42]. However, a problem with the analogue circuitry and a separate problem with the analogue-to-digital converter of TANSO-FTS caused a non-linear response of the signal chains in the TANSO-FTS Band 1 [43,44]. After Version

141.141 of the TANSO-FTS L1B spectra, the analogue circuit non-linearity was corrected, but the non-linearity of the analogue-to-digital converter was not corrected [45]. As reported by Butz *et al.* [21], the response of the non-linearity of TANSO-FTS L1B at Band 1 can be corrected by including a wavenumber-independent offset at the O_2-A band radiance, referred to as a zero-level offset.

In retrievals using real TANSO-FTS L1B spectra, as in the state vector settings described in the previous section, the CO_2 profiles were simultaneously retrieved with the H_2O profile scaling factor, surface pressure, temperature shift, AOD profile, wavenumber shift and squeeze and surface albedo. In addition, the zero-level offset at the O_2-A band was included as a state vector to enable consideration of the non-linear response of TANSO-FTS. *A priori* and covariance matrices of the state vector are identical to those stated in the previous section, with the exception of the zero-level offset. The impact of the zero-level offset is modelled as a simple constant radiance, which is then added to the spectrum. To apply a loose *a priori* constraint, the *a priori* value of the zero-level offset was assumed to be zero. As stated above, our retrieval algorithm considers three aerosol types in the forward model. Aerosol type was determined in the forward model, when the cost function between measured and simulated radiance spectra was minimized among the three aerosol types.

4.2. Comparison of Ground-Based FTS Data and XCO_2 Retrievals

Our retrievals were validated using ground-based FTS (g-b FTS) measurements from TCCON, showing an accuracy of ~0.8 ppm [46]. The measured spectra with ground-based FTS were analysed using a nonlinear least-squares spectral fitting algorithm (GFIT) at JPL, which is used for retrievals across all stations that comprise the TCCON [47,48]. Two TCCON sites over East Asia were selected for validating our retrievals from GOSAT TANSO-FTS, the Saga (33.24°N, 130.29°E) and Tsukuba (36.0°N, 140.12°E) stations. Table 6 provides information about the two TCCON stations used in the study.

Table 6. Ground-based FTS sites used for CO_2 retrievals.

Site	Country	Location	Altitude (m)
Saga	Japan	33.24°N, 130.29°E	7
Tsukuba	Japan	36.05°N, 140.12°E	31

The data analysis software (GGG) commonly used in TCCON was recently updated from its previous version of GGG2012 to the latest version of GGG2014. In this study, we used the GGG2014 datasets to validate our retrievals with g-b FTS. As reported previously [22,49,50], the TCCON data used in this study represent the mean values measured at each TCCON site within $\pm$1 h of the GOSAT overpass time (around 13:00 local time). The XCO_2 values retrieved from our algorithm were selected from boxed latitude/longitude regions within retrieved from our at the Saga and Tsukuba stations, respectively.

Figure 7 shows the comparison of XCO_2 retrieved from our algorithm (YCAR) with the g-b FTS at each TCCON station. In addition, the retrieval results can be compared with the GOSAT Standard Product V02.xx, developed by NIES. To focus on the retrieval accuracy comparison, we retrieved XCO_2 using the spectra that are also retrieved by the NIES algorithm. As shown in Figure 7, the retrieval results at the Saga and Tsukuba sites are biased by 2.78 $\pm$ 1.46 ppm and 1.06 $\pm$ 0.85 ppm, respectively. The YCAR retrievals show larger biases than the NIES retrievals at the Saga site (1.96 $\pm$ 1.26 ppm), but at the Tsukuba site, the accuracy of the YCAR retrievals is slightly better than that of the NIES retrievals (2.18 $\pm$ 1.37 ppm). In addition, the correlation coefficients of the YCAR retrievals at the Saga and Tsukuba sites (0.89 and 0.94, respectively) are higher than those of the NIES retrievals. The standard deviations of the YCAR retrievals at both sites are smaller than those of the NIES retrievals, which indicate that the relative regional-scale accuracy of the YCAR retrievals is better than that of the NIES retrievals in this comparison.

Overall, the XCO_2 retrievals from the YCAR algorithm are in reasonable agreement with the g-b FTS data, although the retrievals still contain some systematic errors that depend on the accuracies of instrument calibrations, the forward model and the assumed model parameters. The errors in instrument calibrations may result from a simple degradation model, which might not represent the actual degradation. In the forward model, we used the recommended scale factors of the O_2 and CO_2 absorption coefficients given in the ABSCO table, as stated by Payne and Thompson [35]. However, the scale factors of the O_2 and CO_2 absorption coefficients depend on the forward model, in which inaccurate coefficients can lead to errors in the retrievals. These errors can be removed by adjusting the absorption cross-section of O_2 and CO_2 throughout the simultaneous retrievals of the scale factors for the O_2 and CO_2 absorption coefficients. In addition, as stated above, the assumed aerosol information can result in systematic errors as the model parameters in the forward model. In the future, to reduce the XCO_2 retrieval errors caused by aerosol information, we plan to investigate the interferences by aerosols using aerosol Lidar or sky-radiometers at selected FTS sites. In addition, it is desirable to improve our algorithm by modifying state vectors for the aerosol-related parameters used in the forward model to reduce errors caused by simplified aerosol information.

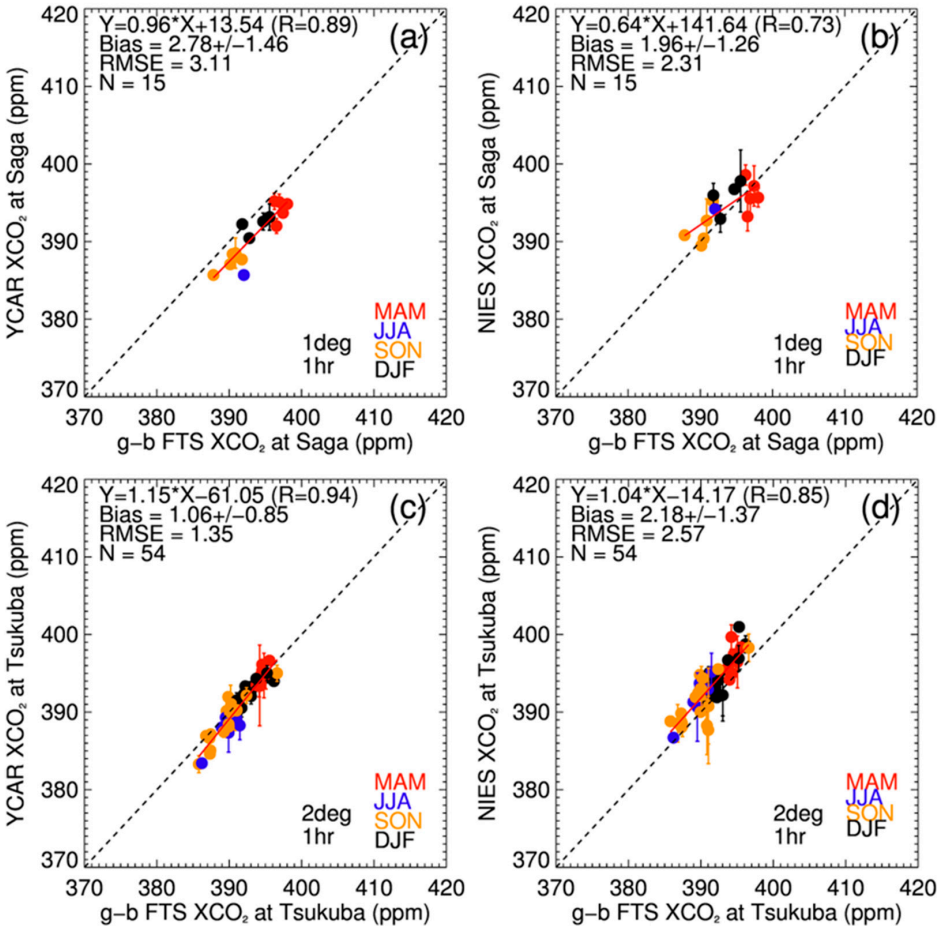

Figure 7. The comparison of XCO_2 retrieved from YCAR and the National Institute for Environment Studies (NIES) algorithm with ground-based FTS: (**a**) YCAR and (**b**) NIES retrievals at Saga station; (**c**) YCAR and (**d**) NIES retrievals at Tsukuba station.

5. Summary and Conclusion

A CO_2 retrieval algorithm, developed using the SWIR channel from GOSAT TANSO-FTS, was examined in this study. To examine the characteristics of the algorithm, we analysed the XCO_2 retrieval errors and averaging kernels using simulated spectra for different AOD and SZA values

and for different aerosol and surface types. It was assumed that the forward model describes the measurements and that the retrieval converges on a final solution in the inverse model.

When calculating XCO_2 retrieval errors and the column averaging kernels in the reference test, several assumptions were applied, including constant atmospheric and vertical AOD profiles and the presence of three aerosol types under cloud-free conditions. Overall, the XCO_2 retrieval errors were small, but varied as a function of AOD, SZA and surface type. However, for the dust aerosol types, the retrieval errors were larger than those for the BC and NA aerosol type, and the patterns of the retrieval errors for the BC and NA aerosol types also varied. Over vegetation and snow surfaces, while the retrieval errors for the BC and NA aerosol types were insensitive to AOD, those for dust were sensitive to both AOD and to SZA. Over the ocean, the retrieval errors increase with increasing AOD and decreasing SZA for all aerosol types, especially as shown for the dust aerosol type. The column averaging kernels are close to unity near the surface over vegetation and snow surfaces and decrease with increasing altitude. Over snow surfaces, the column averaging kernels for the dust type peaks at ~800 hPa, near the top of the aerosol layer, due to the increasing influence of atmospheric scattering. This tendency appears more significant over snow than over vegetation. Over the ocean, the column averaging kernels for all aerosol types show lower values near the surface than at higher altitudes, due to the low surface albedo.

We also examined the influence of each state vector element on the XCO_2 retrieval errors by adding a perturbation to each element. The sensitivity analysis of each state vector to the XCO_2 retrieval errors shows the differences in the CO_2, H_2O and temperature profiles, and total AOD has little influence on the XCO_2 retrieval errors, with resultant errors of only ~0.2 ppm. Aerosol optical properties, on the other hand, have a significant influence on the XCO_2 retrievals. For example, differences in the size distribution of aerosols (fine *versus* coarse particles) can cause errors of up to ~2.5 ppm. Therefore, the sensitivity analysis has shown that of all the state vector elements, the aerosol type information has the greatest influence on the XCO_2 retrievals.

The retrieval algorithm was also tested using real TANSO-FTS L1B spectra and validated with ground-based FTS data at the Saga and Tsukuba TCCON sites. The retrieval results showed a bias by 2.78 and 1.06 ppm at the Saga and Tsukuba sites, respectively. It should be noted that there were biases similar to those of the GOSAT standard products at the Saga and Tsukuba sites, respectively. However, the correlation coefficients at all sites are higher than those obtained using standard products.

Aerosol optical properties can be determined by the refractive index and volume size distribution of particles, which are input parameters in the forward model. Through an extension of our method for calculating the XCO_2 retrieval errors and column averaging kernels, we found that the most important parameters in the forward model are the aerosol optical properties. Recently, we also developed an aerosol retrieval algorithm using TANSO-CAI, which can provide the total AOD and optical properties of aerosols, including fine mode fraction and radiative absorptivity. Compared to other retrieval algorithms, the aerosol information from the CAI is combined with our CO_2 retrieval algorithm, which is up to date and then is expected to improve the accuracy of the CO_2 retrieval algorithm and to provide useful information for estimating the effects of aerosols on the CO_2 retrieval algorithm.

Acknowledgments: This work was supported by National Institute of Meteorological Sciences (NIMS) Research Grant "Development and Application of Methodology for Climate Change Prediction" and the Eco Innovation Program of Korea Environmental Industry & Technology Institute (KEITI, 2012000160002). The authors appreciate the GOSAT Science team of NIES and JAXA Earth Observation Research Center (EORC), Japan, and Yukio Yoshida, Akihiko Kuze and Tatsuya Yokota in particular for useful discussions and immeasurable help with this work. We also appreciate TCCON for providing FTS data obtained from the TCCON Data Archive, operated by the California Institute of Technology, and Shuji Kawakami and Isamu Morino for the use of TCCON dataset at Saga and Tsukuba.

Author Contributions: Y.J. and W.K. worked on the algorithm development and simulation experiments. J.K., H.B., and H.L. conceived and guided the algorithm design. C.C. and T.-Y.G. provided the Carbon Tracker data and user requirements. The authors declare no conflict of interest.

Conflicts of Interest: The authors declare no conflict of interest.

References

1. Stocker, T.F.; Qin, D.; Plattner, G.-K.; Tignor, M.; Allen, S.K.; Boschung, J.; Nauels, A.; Xia, Y.; Bex, V.; Midgley, P.M. *Climate Change 2013. The Physical Science Basis*; Working Group I Contribution to the Fifth Assessment Report of the Intergovernmental Panel on Climate Change; Cambridge University Press: Cambridge, UK, 2013.
2. Friedlingstein, P.; Meinshausen, M.; Arora, V.K.; Jones, C.D.; Anav, A.; Liddicoat, S.K.; Knutti, R. Uncertainties in CMIP5 climate projections due to carbon cycle feedbacks. *J. Clim.* **2014**, *27*, 511–526. [CrossRef]
3. Rayner, P.J.; O'Brien, D.M. The utility of remotely sensed CO_2 concentration data in surface source inversions. *Geophys. Res. Lett.* **2001**, *28*, 175–178. [CrossRef]
4. Crevoisier, C.; Heilliette, S.; Chédin, A.; Serrar, S.; Armante, R.; Scott, N.A. Midtropospheric CO_2 concentration retrieval from AIRS observations in the tropics. *Geophys. Res. Lett.* **2004**, *31*. [CrossRef]
5. Buchwitz, M.; De Beek, R.; Noël, S.; Burrows, J.P.; Bovensmann, H.; Schneising, O.; Khlystova, I.; Bruns, M.; Bremer, H.; Bergamaschi, P.; *et al.* Atmospheric carbon gases retrieved from SCIAMACHY by WFM-DOAS: version 0.5 CO and CH_4 and impact of calibration improvements on CO_2 retrieval. *Atmos. Chem. Phys.* **2006**, *6*, 2727–2751. [CrossRef]
6. Barkley, M.P.; Friess, U.; Monks, P.S. Measuring atmospheric CO_2 from space using Full Spectral Initiation (FSI) WFM-DOAS. *Atmos. Chem. Phys.* **2006**, *6*, 3517–3534. [CrossRef]
7. Bösch, H.; Toon, G.C.; Sen, B.; Washenfelder, R.A.; Wennberg, P.O.; Buchwitz, M.; De Beek, R.; Burrows, J.P.; Crisp, D.; Christi, M.; *et al.* Space-based near-infrared CO_2 measurements: Testing the Orbiting Carbon Observatory retrieval algorithm and validation concept using SCIAMACHY observations over Park Falls, Wisconsin. *J. Geophys. Res.* **2006**, *111*. [CrossRef]
8. Yokota, T.; Yoshida, Y.; Eguchi, N.; Ota, Y.; Tanaka, T.; Watanabe, H.; Maksyutov, S. Global concentrations of CO_2 and CH_4 retrieved from GOSAT: First preliminary results. *SOLA* **2009**, *5*, 160–163. [CrossRef]
9. Kuze, A.; Suto, H.; Nakajima, M.; Hamazaki, T. Thermal and near infrared sensor for carbon observation Fourier-transform spectrometer on the Greenhouse Gases Observing Satellite for greenhouse gases monitoring. *Appl. Opt.* **2009**, *48*, 6716–6733. [CrossRef] [PubMed]
10. Yoshida, Y.; Ota, Y.; Eguchi, N.; Kikuchi, N.; Nobuta, K.; Tran, H.; Morino, I.; Yokota, T. Retrieval algorithm for CO_2 and CH_4 column abundances from short-wavelength infrared spectral observations by the Greenhouse gases observing satellite. *Atmos. Meas. Tech.* **2011**, *4*, 717–734. [CrossRef]
11. Bril, A.; Oshchepkov, S.; Yokota, T.; Inoue, G. Parameterization of aerosol and cirrus cloud effects on reflected sunlight spectra measured from space: Application of the equivalence theorem. *Appl. Opt.* **2007**, *46*, 2460–2470. [CrossRef] [PubMed]
12. Oshchepkov, S.; Bril, A.; Yokota, T. PPDF-based method to account for atmospheric light scattering in observations of carbon dioxide from space. *J. Geophys. Res.* **2008**, *113*. [CrossRef]
13. Oshchepkov, S.; Bril, A.; Yokota, T. An improved photon path length probability density function–based radiative transfer model for space-based observation of greenhouse gases. *J. Geophys. Res.* **2009**, *114*, D19207. [CrossRef]
14. Oshchepkov, S.; Bril, A.; Maksyutov, S.; Yokota, T. Detection of optical path in spectroscopic space-based observations of greenhouse gases: Application to GOSAT data processing. *J. Geophys. Res.* **2011**, *116*, D14304. [CrossRef]
15. Crisp, D.; Fisher, B.; O'Dell, C.; Frankenberg, C.; Basilio, R.; Bosch, H.; Brown, L.R.; Castano, R.; Connor, B.; Deutscher, N.M.; *et al.* The ACOS CO_2 retrieval algorithm-Part II: Global XCO_2 data characterization. *Atmos. Meas. Tech.* **2012**, *5*, 687–707. [CrossRef]
16. O'Dell, C.W.; Connor, B.; Bösch, H.; O'Brien, D.; Frankenberg, C.; Castano, R.; Christi, M.; Eldering, D.; Fisher, B.; Gunson, M.; *et al.* The ACOS CO_2 retrieval algorithm–Part 1: Description and validation against synthetic observations. *Atmos. Meas. Tech.* **2012**, *5*, 99–121. [CrossRef]
17. Boesch, H.; Baker, D.; Connor, B.; Crisp, D.; Miller, C. Global characterization of CO_2 column retrievals from shortwave-infrared satellite observations of the Orbiting Carbon Observatory-2 mission. *Remote Sens.* **2011**, *3*, 270–304. [CrossRef]
18. Connor, B.J.; Boesch, H.; Toon, G.; Sen, B.; Miller, C.; Crisp, D. Orbiting Carbon Observatory: Inverse method and prospective error analysis. *J. Geophys. Res.* **2008**, *113*. [CrossRef]

19. Butz, A.; Hasekamp, O.; Frankenberg, C.; Aben, I. Retrievals of atmospheric CO_2 from simulated space-borne measurements of backscattered near-infrared sunlight: Accounting for aerosol effects. *Appl. Opt.* **2009**, *48*, 3322–3336. [CrossRef] [PubMed]
20. Butz, A.; Hasekamp, O.; Frankenberg, C.; Vidot, J.; Aben, I. CH_4 retrievals from space-based solar backscatter measurements: Performance evaluation against simulated aerosol and cirrus loaded scenes. *J. Geophys. Res.* **2010**, *115*. [CrossRef]
21. Butz, A.; Guerlet, S.; Hasekamp, O.; Schepers, D.; Galli, A.; Aben, I.; Frankenberg, C.; Hartmann, J.M.; Tran, H.; Kuze, A.; *et al.* Toward accurate CO_2 and CH_4 observations from GOSAT. *Geophys. Res. Lett.* **2011**, *38*, L14812. [CrossRef]
22. Heymann, J.; Reuter, M.; Hilker, M.; Buchwitz, M.; Schneising, O.; Bovensmann, H.; Burrows, J.; Kuze, A.; Suto, H.; Deutscher, N.M.; *et al.* Consistent satellite XCO_2 retrievals from SCIAMACHY and GOSAT using the BESD algorithm. *Atmos. Meas. Tech.* **2015**, *8*, 2961–2980. [CrossRef]
23. Rodgers, C.D. *Inverse Methods for Atmospheric Sounding: Theory and Practice*, 2nd ed.; World Scientific Publishig Co. Pte. Ltd.: Singapore, 2000.
24. Oshchepkov, S.; Bril, A.; Yokota, T.; Morino, I.; Yoshida, Y.; Matsunaga, T.; Belikov, D.; Wunch, D.; Wennberg, P.; Toon, G.; *et al.* Effects of atmospheric light scattering on spectroscopic observations of greenhouse gases from space: Validation of PPDF-based CO_2 retrievals from GOSAT. *J. Geophys. Res.* **2012**, *117*, D12305. [CrossRef]
25. O'Brien, D.M.; Rayner, P.J. Global observations of the carbon budget, 2, CO_2 column from differential absorption of reflected sunlight in the 1.61 μm band of CO_2. *J. Geophys. Res.* **2002**, *107*, 4354. [CrossRef]
26. Carbon Tracker-Asia Webpage. Available online: http://www.nimr.go.kr/2/carbontracker/index.html (accessed on 10 April 2016).
27. Carbon Tracker Webpage. Available online: http://www.esrl.noaa.gov/gmd/ccgg/carbontracker/ (accessed on 10 April 2016).
28. Hong, S.-Y.; Noh, Y.; Dudhia, J. A new vertical diffusion package with an explicit treatment of entrainment processes. *Mon. Weather Rev.* **2006**, *134*, 2318–2341. [CrossRef]
29. Salstein, D.A.; Ponte, R.M.; Cady-Pereira, K. Uncertainties in atmospheric surface pressure fields from global analyses. *J. Geophys. Res.* **2008**, *113*. [CrossRef]
30. Dubovik, O.; King, M.D. A flexible inversion algorithm for retrieval of aerosol optical properties from Sun and sky radiance measurements. *J. Geophys. Res.* **2000**, *105*, 20673–20696. [CrossRef]
31. Kim, J.; Lee, J.; Lee, H.C.; Higurashi, A.; Takemura, T.; Song, C.H. Consistency of the aerosol type classification from satellite remote sensing during the Atmospheric Brown Cloud–East Asia Regional Experiment campaign. *J. Geophys. Res.* **2007**, *112*, D22S33. [CrossRef]
32. Lee, J.; Kim, J.; Song, C.; Kim, S.; Chun, Y.; Sohn, B.; Holben, B. Characteristics of aerosol types from AERONET sunphotometer measurements. *Atmos. Environ.* **2010**, *44*, 3110–3117. [CrossRef]
33. Spurr, R.J. VLIDORT: A linearized pseudo-spherical vector discrete ordinate radiative transfer code for forward model and retrieval studies in multilayer multiple scattering media. *J. Quant. Spectrosc. Radiat. Transf.* **2006**, *102*, 316–342. [CrossRef]
34. Crisp, D.; Bösch, H.; Brown, L.; Castano, R.; Christi, M.; Connor, B.; Frankenberg, C.; McDuffie, J.; Miller, C.; Natraj, V. OCO (Orbiting Carbon Observatory)-2 Level 2 Full Physics Retrieval Algorithm Theoretical Basis. Available online: http://disc.sci.gsfc.nasa.gov/acdisc/documentation/OCO-2_L2_FP_ATBD_v1_rev4_Nov10.pdf (accessed on 10 November 2010).
35. Payne, V.; Thompson, D. Spectroscopic needs for OCO-2. Available online: https://oco.jpl.nasa.gov/files/ocov2/OCO-2_spectroscopic_needs_20132.pdf (accessed on 3 December 2013).
36. Tran, H.; Hartmann, J. An improved O_2 A band absorption model and its consequences for retrievals of photon paths and surface pressures. *J. Geophys. Res.* **2008**, *113*, D18104. [CrossRef]
37. Bodhaine, B.A.; Wood, N.B.; Dutton, E.G.; Slusser, J.R. On Rayleigh optical depth calculations. *J. Atmos. Ocean. Technol.* **1999**, *16*, 1854–1861. [CrossRef]
38. Thuillier, G.; Herse, M.; Labs, S.; Foujols, T.; Peetermans, W.; Gillotay, D.; Simon, P.C.; Mandel, H. The solar spectral irradiance from 200 to 2400 nm as measured by the SOLSPEC Spectrometer from the ATLAS 123 and EURECA missions. *Sol. Phys.* **2003**, *214*, 1–22. [CrossRef]
39. Baldridge, A.; Hook, S.; Grove, C.; Rivera, G. The ASTER spectral library version 2.0. *Remote Sens. Environ.* **2009**, *113*, 711–715. [CrossRef]

40. Kahn, R.; Banerjee, P.; McDonald, D. Sensitivity of multiangle imaging to natural mixtures of aerosols over ocean. *J. Geophys. Res.* **2001**, *106*, 18219–18238. [CrossRef]
41. Yoshida, Y.; Kikuchi, N.; Yokota, T. On-orbit radiometric calibration of SWIR bands of TANSO-FTS onboard GOSAT. *Atmos. Meas. Tech.* **2012**, *5*, 2515–2523. [CrossRef]
42. Kuze, A.; Taylor, T.E.; Kataoka, F.; Bruegge, C.J.; Crisp, D.; Harada, M.; Helmlinger, M.; Inoue, M.; Kawakami, S.; Kikuchi, N. Long-term vicarious calibration of GOSAT short-wave sensors: Techniques for error reduction and new estimates of radiometric degradation factors. *IEEE Trans. Geosci. Remote Sens.* **2014**, *52*, 3991–4004. [CrossRef]
43. Kuze, A.; Suto, H.; Shiomi, K.; Urabe, T.; Nakajima, M.; Yoshida, J.; Kawashima, T.; Yamamoto, Y.; Kataoka, F.; Buijs, H. Level 1 algorithms for TANSO on GOSAT: Processing and on-orbit calibrations. *Atmos. Meas. Tech.* **2012**, *5*, 2447–2467. [CrossRef]
44. Suto, H.; Kuze, A.; Shiomi, K.; Nakajima, M. Updated level-1 processing after two-years operation of TANSO-FTS. *Proc. SPIE* **2011**. [CrossRef]
45. Yoshida, Y.; Kikuchi, N.; Morino, I.; Uchino, O.; Oshchepkov, S.; Bril, A.; Saeki, T.; Schutgens, N.; Toon, G.; Wunch, D. Improvement of the retrieval algorithm for GOSAT SWIR XCO_2 and XCH_4 and their validation using TCCON data. *Atmos. Meas. Tech.* **2013**, *6*, 1533–1547. [CrossRef]
46. Wunch, D.; Toon, G.C.; Wennberg, P.O.; Wofsy, S.C.; Stephens, B.B.; Fischer, M.L.; Uchino, O.; Abshire, J.B.; Bernath, P.; Biraud, S.C.; *et al.* Calibration of the Total Carbon Column Observing Network using aircraft profile data. *Atmos. Meas. Tech.* **2010**, *3*, 1351–1362. [CrossRef]
47. Toon, G.; Farmer, C.; Schaper, P.; Lowes, L.; Norton, R. Composition measurements of the 1989 Arctic winter stratosphere by airborne infrared solar absorption spectroscopy. *J. Geophys. Res.* **1992**, *97*, 7939–7961. [CrossRef]
48. Wunch, D.; Toon, G.C.; Blavier, J.-F.L.; Washenfelder, R.A.; Notholt, J.; Connor, B.J.; Griffith, D.W.; Sherlock, V.; Wennberg, P.O. The total carbon column observing network. *Philos. Trans. R. Soc. A* **2011**, *369*, 2087–2112. [CrossRef] [PubMed]
49. Morino, I.; Uchino, O.; Inoue, M.; Yoshida, Y.; Yokota, T.; Wennberg, P.; Toon, G.; Wunch, D.; Roehl, C.; Notholt, J.; *et al.* Preliminary validation of column-averaged volume mixing ratios of carbon dioxide and methane retrieved from GOSAT short-wavelength infrared spectra. *Atmos. Meas. Tech.* **2010**, *4*, 1061–1076. [CrossRef]
50. Guerlet, S.; Butz, A.; Schepers, D.; Basu, S.; Hasekamp, O.; Kuze, A.; Yokota, T.; Blavier, J.F.; Deutscher, N.; Griffith, D.T.; *et al.* Impact of aerosol and thin cirrus on retrieving and validating XCO_2 from GOSAT shortwave infrared measurements. *J. Geophys. Res.* **2013**, *118*, 4887–4905. [CrossRef]